Delft University of Technology

On the high temperature oxidation of $MoSi_2$ particles with boron addition

Ding, Zhaoying; Brouwer, Johannes C.; Yao, Xiyu; Zhu, Jia Ning; Hermans, Marcel J.M.; Popovich, Vera; Sloof, Willem G.

DOI
10.1016/j.jeurceramsoc.2024.05.002

Publication date
2024

Document Version
Final published version

Published in
Journal of the European Ceramic Society

Citation (APA)
Ding, Z., Brouwer, J. C., Yao, X., Zhu, J. N., Hermans, M. J. M., Popovich, V., & Sloof, W. G. (2024). On the high temperature oxidation of $MoSi_2$ particles with boron addition. *Journal of the European Ceramic Society*, *44*(12), 7170-7179. https://doi.org/10.1016/j.jeurceramsoc.2024.05.002

Important note
To cite this publication, please use the final published version (if applicable).
Please check the document version above.

Copyright
Other than for strictly personal use, it is not permitted to download, forward or distribute the text or part of it, without the consent of the author(s) and/or copyright holder(s), unless the work is under an open content license such as Creative Commons.

Takedown policy
Please contact us and provide details if you believe this document breaches copyrights.
We will remove access to the work immediately and investigate your claim.

This work is downloaded from Delft University of Technology.
For technical reasons the number of authors shown on this cover page is limited to a maximum of 10.

Journal of the European Ceramic Society 44 (2024) 7170–7179

Contents lists available at ScienceDirect

Journal of the European Ceramic Society

journal homepage: www.elsevier.com/locate/jeurceramsoc

On the high temperature oxidation of $MoSi_2$ particles with boron addition

Zhaoying Ding [a], Johannes C. Brouwer [a], Xiyu Yao [b], Jia-Ning Zhu [a], Marcel J.M. Hermans [a], Vera Popovich [a], Willem G. Sloof [a,*]

[a] Department of Materials Science and Engineering, Delft University of Technology, Mekelweg 2, Delft 2628 CD, the Netherlands
[b] Department of Materials Science and Engineering, Southern University of Science and Technology, Shenzhen 518055, China

ARTICLE INFO

Keywords:
$MoSi_2$
Particles
Boron
Oxidation
Kinetics

ABSTRACT

Boron doped $MoSi_2$ particles have been envisioned as sacrificial particles for self-healing thermal barrier coatings (TBCs) but their oxidation behaviour is yet not well understood. In this work, oxidation of $MoSi_2$ based particle is studied in the temperature range of 1050–1200 °C. The oxidation proceeds from a transient to a steady-state oxidation stage. The kinetics during steady-state oxidation is captured with a thermal diffusion-based model. As compared to the oxidation of pure $MoSi_2$ particles, the addition of boron strongly enhances the silica formation. Also, a finer dispersion of MoB_x in the $MoSi_2$ matrix accelerates the formation of silica. The oxide growth rate constant increases proportional with the boron content of the $MoSi_2$ particles. This enhanced oxidation is related to the microstructure of the oxide scale. Upon oxidation, boron yields B_2O_3, which promptly merge with SiO_2 to form amorphous borosilicate, hindering the formation of crystalline SiO_2. Consequently, the migration of oxygen in the borosilicate oxide scale is faster than in the silica oxide scale on pure $MoSi_2$ particles.

1. Introduction

With a melting point over 2000 °C, moderate density (6.3 g cm^{-3}), and outstanding oxidation resistance, molybdenum disilicide ($MoSi_2$) is an attractive material for high-temperature applications such as heating elements, protective coatings, engines parts, *etc* [1–3]. Moreover, particles of $MoSi_2$ with small amounts of boron are envisioned as sacrificial particles for self-healing thermal barrier coatings (TBCs) [4–6]. Then, these particles are embedded in yttria partially stabilized zirconia (YPSZ) [4]. Once intercepted by cracks [7,8], the $MoSi_2$ based particles oxidize preferentially and the oxidation product of amorphous SiO_2 fills the crack gaps and subsequently reacts with ZrO_2 of the YPSZ matrix to form $ZrSiO_4$ at the crack face surfaces restoring the mechanical integrity [4–6,9]. In this context, the presence of boron in the $MoSi_2$ particles is paramount for crack healing since it increases the fluidity of the SiO_2 [4] and promotes the subsequent reaction with ZrO_2 to form the load-bearing phase of $ZrSiO_4$ [9]. Therefore, adding a small amount of boron in $MoSi_2$ particle becomes imperative in a self-healing TBC system, where the precise amount of boron addition holds the key to regulating the healing rate [10,11].

The oxidation behaviour of bulk $MoSi_2$ in the temperature range of 400–1800 °C has been well documented [2,3,12–16]. However, the oxidation behaviour of $MoSi_2$ particles is rarely reported. In contrast with the oxidation of the bulk $MoSi_2$ [17,18], the oxidation process of $MoSi_2$ based particles is much more complex due to stronger element depletion, larger specific surface area and associated higher defect density of particles [19,20]. When boron is added to $MoSi_2$ particles, knowledge about their oxidation behaviour is lacking. However, for the high temperature oxidation of bulk Mo–Si–B alloys [21–26], it has been reported that the oxidation significantly accelerated by adding a small trace of B [27].

This work focuses on the oxidation of two-phase $MoSi_2$–MoB_x particles. The oxidation of $MoSi_2$ particles with and without boron doping was investigated in the temperature range from 1050 up to 1200 °C. The effects of particle size, boron content and microstructure on the oxidation kinetics were studied at 1100 °C. The microstructure evolution of the oxide scale was investigated to reveal the oxidation mechanism.

2. Materials and methods

2.1. Particle preparation

2.1.1. Starting material

$MoSi_2$ powders with and without boron (< 45 μm, ChemPUR GmbH, Germany) were used as the starting material. This starting material is wind-sifted to eliminate the extremely fine fraction of the particles; see

* Corresponding author.
E-mail address: w.g.sloof@tudelft.nl (W.G. Sloof).

https://doi.org/10.1016/j.jeurceramsoc.2024.05.002
Received 13 January 2024; Received in revised form 10 April 2024; Accepted 1 May 2024
Available online 9 May 2024
0955-2219/© 2024 The Author(s). Published by Elsevier Ltd. This is an open access article under the CC BY license (http://creativecommons.org/licenses/by/4.0/).

the particle size distribution in Fig. S1. Wind sifting was performed using an Alpine 100 MRZ laboratory zig-zag classifier (Alpine Multi-Plex 100 MRZ, Hosokawa Micron Powder System, USA) with the airflow fixed at 15 m^3 h^{-1} and the classifier rotational speed kept at 5000 rpm. To confirm the boron content of the material, the wind-sifted particles were analysed using inductively couple plasma optical emission spectroscopy (ICP-OES, using iCAP 6500 Duo, Thermo Fisher Scientific). The dissolution process was specifically designed for the Mo–Si–B system [28]. The measured content of boron is 1.3 wt% (6 at.%), which is lower than the nominal 2 wt%; see Table 1. Henceforth, the particles are denoted as wind-sifted Mo–67Si and wind-sifted Mo–58Si–6B, respectively.

2.1.2. Particles with different sizes

To investigate the influence of particle size on the oxidation kinetics, different size fractions of the wind-sifted Mo–58Si–6B particles were prepared via sieving the particles through 20 and 50 μm sieves (Analysensieb, DIN-ISO 3310–1, Retsch, Germany). Thus, fine particles with a size of $d < 20$ μm and particles with a size of $20 < d < 50$ μm were obtained. The coarse particles ($d > 50$ μm) were discarded. In the end, three batches of particles with different sizes distribution were prepared, namely wind-sifted particles containing a mixture of fine and coarse particles, fine fraction of the sieved particles with particle size of $d <$ 20 μm and sieved particles with particle size of $20 < d < 50$ μm. Their morphologies and size distribution are shown in Fig. 1a–f.

In order to confirm the boron content of the particles with different sizes, ICP-OES analysis was conducted according to the same procedure as mentioned in Section 2.1.1; see Table 1. The boron content of particles with different sizes do not differ much.

2.1.3. Particles with various boron content

A mixture of the starting powders, i.e., $MoSi_2$ without and with 6 at.% B, with a ratio of 1:1 were prepared to obtain $MoSi_2$ with 3 at.% B particles. To refine the dispersion of the MoB phase in the particles, the starting powders and their mixtures were milled using a planetary ball mill (PM100, Retsch GmbH, Germany). Wet ball-milling of the powders was conducted in isopropanol using zirconia balls (100 and 8 balls with diameter of 5 and 10 mm, respectively) and a zirconia jar (50 ml). The weight ratio between balls and powder was about 5:1. The milling speed was 300 rpm and the milling time was 3 hours with cycles of 20 minutes running and 10 minutes pause, i.e., the effective milling time was 2 hours. Subsequently, the milled powder was dried in the oven for 12 hours at 80 °C. The dried powder was then sieved with a 200 μm mesh sieve. ICP-OES analysis was conducted according to the same procedure as mentioned in Section 2.1.1 and the as determined boron content of the ball milled powders was 3 and 6 at.% respectively, demonstrating that there is no significant loss of boron in the ball milling process; see Table 1.

Next, the above ball milled powders were densified by means of spark plasma sintering (SPS) with a HP D 25 SD furnace (FCT Systeme GmbH, Germany) at 1500 °C for 30 minutes in a flowing argon atmosphere with a pressure of 50 MPa. The heating was 20 °C min^{-1}, while natural cooling was used to cool down from the sintering temperature to room temperature.

Table 1
Summary of prepared particles and their corresponding processing conditions.

Nominal composition (-)	Pre-treatment (-)	Boron content (wt%)	Actual composition (-)
$MoSi_2$	Wind-sifted	0.0	Mo–67Si
$MoSi_2$-2 wt% B	Wind-sifted	1.3	Mo–58Si–6B
	Sieved $20 < d <$ 50 μm	1.4	Mo–58Si–7B
	Sieved $d < 20$ μm	1.5	Mo–57Si–7B
$MoSi_2$	Refined and spheroidized	/	Mo–67Si
$MoSi_2$-1 wt% B	Refined and spheroidized	0.7	Mo–63Si–3B
$MoSi_2$-2 wt% B	Refined and spheroidized	1.3	Mo–59Si–6B

The microstructure of the densified material prepared by SPS of the as received and ball milled $MoSi_2$ based powders is shown in Fig. 2. It is evident that the ball milling treatment of the $MoSi_2$ based powders promotes an even and fine distribution of the boride phase; comparing Figs. 2c and 2d with Fig. 2b. Inclusion of SiO_2 can be observed in the microstructures in Fig. 2 but cannot be seen in the diffractograms, indicating an amorphous nature. The formation of SiO_2 is attributed to residual oxygen that still exists (~1000 ppm) even though the SPS sintering is carried out in a vacuum environment [29,30]. In addition, the wet balling process may have caused substantial amount of adsorbed residual oxygen at the surface of the particles, which led to the formation of some SiO_2 during the sintering process; see Fig. 2c and d.

The dense materials prepared were pulverized and sieved. The pulverizing was done using a Fritsch Pulverisette (type P-0150, Germany) with a steel ball (diameter 70 mm). To spheroidize the crushed powders, a combined ball milling and polishing process was executed. Full details of the particle processing procedure can be found in [18]. The morphology of the spheroidized particles is shown in Fig. 1g–i. As compared with the starting powders, the size of these particles is more uniform and their shape is more spherical. Transition from MoB_2 to MoB was observed in the microstructure refinement since MoB phase exhibits the lowest energy of formation among all the molybdenum borides [31]; see the diffractograms in Fig. 1j–k. This observation is in agreement with the isothermal section of the Mo–Si–B ternary phase diagram at 1450 °C [32] (close to the sintering temperature of 1500 °C).

2.2. Isothermal high temperature oxidation

The isothermal oxidation kinetics of the $MoSi_2$ based particles at temperatures in the range of 1050–1200 °C in terms of mass change was assessed via thermogravimetric analyses, using a dual furnace balance (Seteram TAG 16/18, France) which allows automatic correction for buoyancy effects. The alumina furnace tubes have an inner diameter of 15 mm. This analyser is equipped with Pt/Pt-10%Rh (S-type) thermocouples. The mass change of the particles was recorded upon oxidation in dry synthetic air (N_2 with 20 vol.% O_2). The gas mixture was admitted to the TGA analyser via mass flow controllers (Bronkhorst, The Netherlands) operated with Labview (version 2020) such that the total gas flow matches 100 sccm, which was equally divided over both furnace tubes. Prior to admitting the gas mixture to the furnace, each gas, i.e., both oxygen and nitrogen (Linde Gas Benelux BV, purity better than 5 N), were filtered to remove any residual moisture and hydrocarbons, with Hydrosorb (< 20 ppb H_2O) and Accosorb (< 10 ppb hydrocarbons) filters (Messer Griesheim, Germany), respectively. The nitrogen gas was additionally filtered to remove residual oxygen with an Oxysorb filter (< 5 ppb O_2).

Approximately 200 mg particles were loaded into a 100 μL alumina crucible. The initial mass of the particles was weighed using a Mettler Toledo mechanical balance (AG-204, Switzerland, accuracy ± 1 μg). The crucible with the particles was mounted at one side of the balance and an identical but empty crucible was mounted at the other side of the balance. Both furnaces, each at one side of the balance, were heated simultaneously with 10 °C min^{-1} in a flow of pure nitrogen. When both furnaces of the thermogravimetric analyser reached the target temperature, oxygen was added to the nitrogen gas flow to create dry synthetic air during the isothermal hold.

2.3. Characterization

The phase composition of the materials was determined with X-ray diffractometry (XRD) using a D8 advance diffractometer (Bruker, Germany) operated with Co Kα radiation. Diffractograms were recorded in the 2θ range of 10–110° with a 2θ step size of 0.030° and a counting time

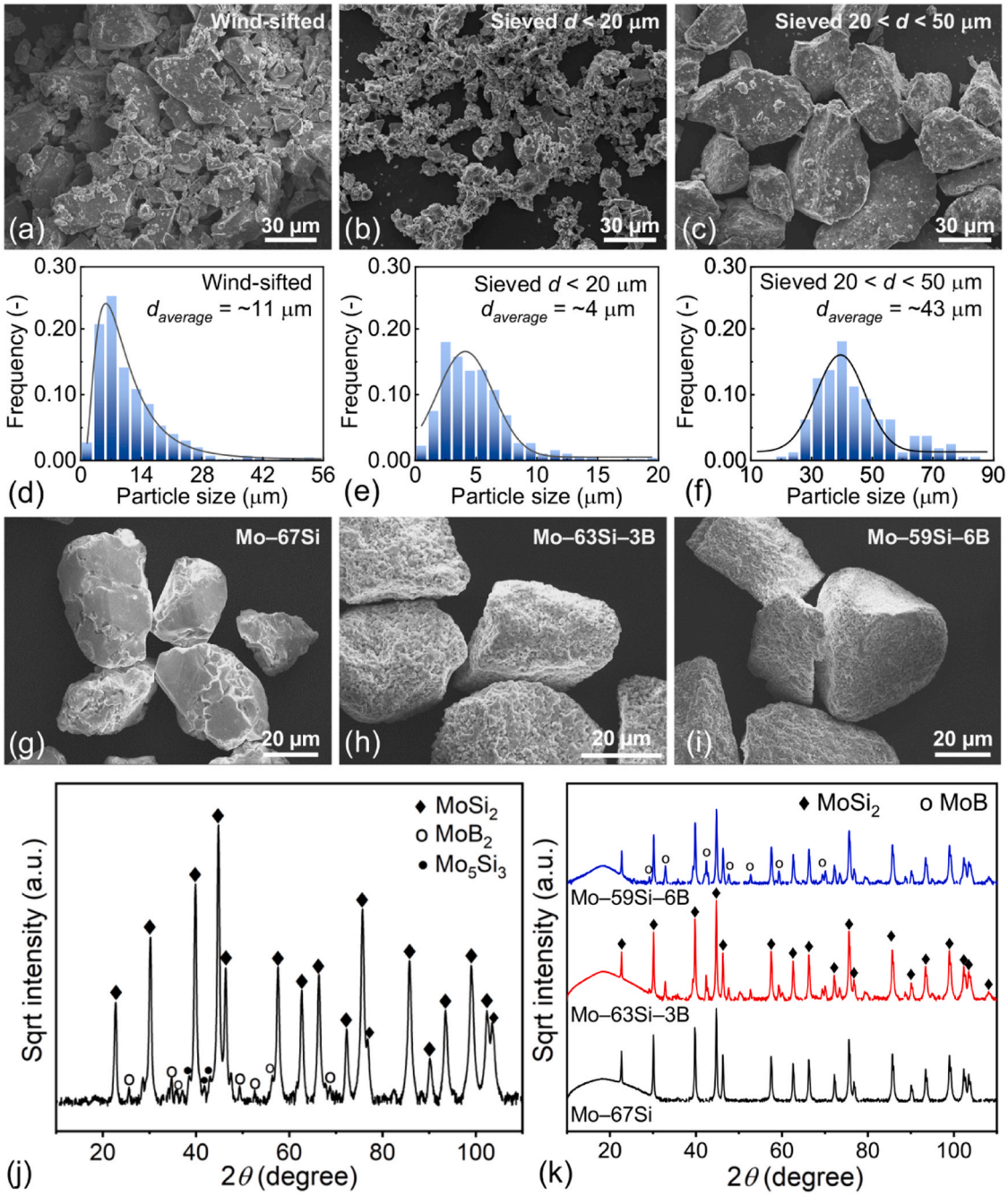

Fig. 1. (a)–(c) SEM images of the morphology of $MoSi_2$ particles with boron addition and different sizes: (a) wind-sifted particles contain a mixture of fine and coarse particles; (b) fine fraction of the sieved particle with particle size of $d < 20$ μm; (c) sieved particle with a uniform particle size of $20 < d < 50$ μm and (d)–(f) the corresponding particle size distribution; (g)–(i) SEM images of the morphology of spheroidized Mo–Si based particles prepared from crunching a SPS tablet and a gentle ball milling and polishing process afterwards; XRD patterns of (j) wind-sifted Mo–58Si–6B particles and (k) spheroidized Mo–Si based particles.

per step of 2 s. These diffractograms were evaluated using the Bruker Diffrac EVA software (version 3.1). The microstructure in terms of boron distribution of the sintered tablets and the morphology of the particles was observed with scanning electron microscopy (SEM) using a JEOL JSM 6500 F (JEOL, Japan). To study the mechanism of boron accelerated $MoSi_2$ particle oxidation, scanning electron microscopy combined with a Xenon plasma focused ion beam (Helios G4 PFIB UXe, Thermo Fisher Scientific, USA) was performed to create cross-sections of the spheroidized particles after oxidation in dry synthetic air for 20 hours. First, the particles to be investigated were put on a silicon wafer (Si-<100> p-type, University Wafer, USA). Next, one of the particles was covered with about 2 μm layer of Pt added with some C using the electron beam operated at 12 keV. Then, the particle was cut with the Xenon plasma focused ion beam operated at 30 keV. Lamella for transmission electron microscopy (TEM) from selected areas in the oxide scale were also prepared with the plasma focused ion beam and subsequently lifted. Next, the thin lamellas were analysed with TEM using a Cs-corrected Titan ETEM G2 apparatus (FEI/Thermo Fisher Scientific, USA) operated at 300 keV, which was equipped with a Gatan K3 camera for performing electron energy loss spectroscopy (EELS). The elemental mapping and energy-dispersive spectroscopy (EDS) spectra were carried out with a Talos F200X field-emission TEM (FEI/Thermo Fisher Scientific, USA) operated at 200 keV, equipped with a high-brightness field emission gun (X-FEG) and a Super-X G2 EDX detector.

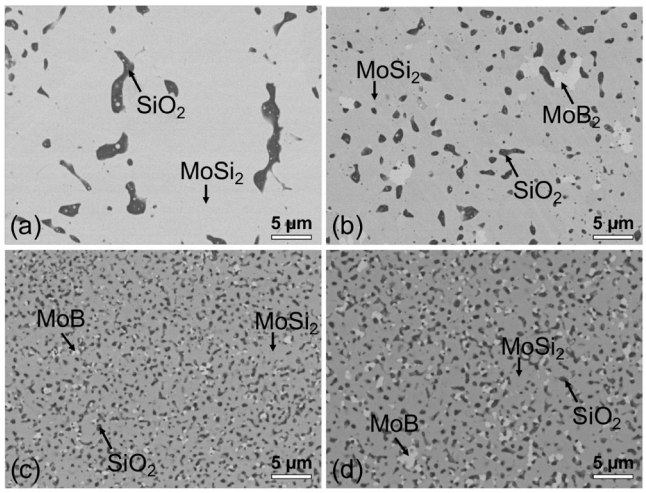

Fig. 2. SEM back scattered electron images of the microstructure of different Mo–Si based bulk materials prepared with SPS from: (a) Mo–67Si particles, (b) as-received Mo–58Si–6B particles, (c) ball milled Mo–64Si–3B particles and (d) ball milled Mo–59Si–6B particles.

3. Results and discussion

3.1. Thermodynamic considerations

The oxidation of pure $MoSi_2$ particles proceeds according to [19]:

$$5MoSi_2(s) + 7O_2(g) \rightarrow Mo_5Si_3(s) + 7SiO_2(s), \quad (1)$$

and Mo_5Si_3 subsequently oxidizes according to [13,19]:

$$Mo_5Si_3(s) + 10.5O_2(g) \rightarrow 5MoO_3(g) + 3SiO_2(s). \quad (2)$$

In the early stage of oxidation, the two reactions are considered to occur simultaneously rather than consecutively [19]. In the following stage, when a continuous SiO_2 passive layer is formed on the surface, the oxidation of Mo_5Si_3, i.e. Eq. (2), is suppressed [19]. This two-step oxidation process of pure $MoSi_2$ particles is consistent with what is generally accepted for the oxidation of bulk $MoSi_2$ [14]. Then, MoO_3 forms initially and evaporates quickly before the formation of a continuous SiO_2 film on $MoSi_2$.

The oxidation of boron in the system considered here proceeds according to [33]:

$$4MoB(s)7O_2 \rightarrow 4MoO_2(g) + 2B_2O_3(g) \quad (3)$$

Given that the free energies of formation of B_2O_3 and SiO_2 are very close [34], Si and B tend to oxidize simultaneously. Once these two oxides are formed (according to Eqs. (1) and (3)), B_2O_3 and SiO_2 merge rapidly to form amorphous borosilicate.

The Mo–O, Si–O, and B–O stability diagrams pertaining to 1100 °C are presented in Fig. 3. It can be seen that the dissociation oxygen partial pressure of the oxides increases in of order SiO_2, B_2O_3, MoO_2, and MoO_3 (10^{-25}, 10^{-23}, 10^{-13} and 10^{-6} atm., respectively). Thus, SiO_2 is the most stable oxide, more than B_2O_3, which is more stable than MoO_2 and MoO_3. According to these stability diagrams (Fig. 3), the major volatile species are the higher order oxides of molybdenum, i.e. $(MoO_3)_2$. During the initial oxidation of pure $MoSi_2$ particles besides silica also volatile Mo-oxides are formed. Once the surfaces of these particles are fully covered with silica or borosilicate, the formation of Mo-oxides is terminated. Then, the oxidation proceeds from the early transient stage to the subsequent steady-state oxidation, during which only Si is selectively oxidized and the oxygen partial pressure at the oxide interface is governed by the equilibrium between Si in the alloy at the interface with the oxide scale composed of SiO_2 (about 10^{-25} atm. at 1100 °C). Therefore, the formation of a continuous SiO_2 or borosilicate scale on the surface marks the transition from a fast initial to a steady-state oxidation of $MoSi_2$ based particles.

3.2. Oxidation kinetics

The rate of conversion into oxides upon thermal oxidation of the solid particles can be described with [35]:

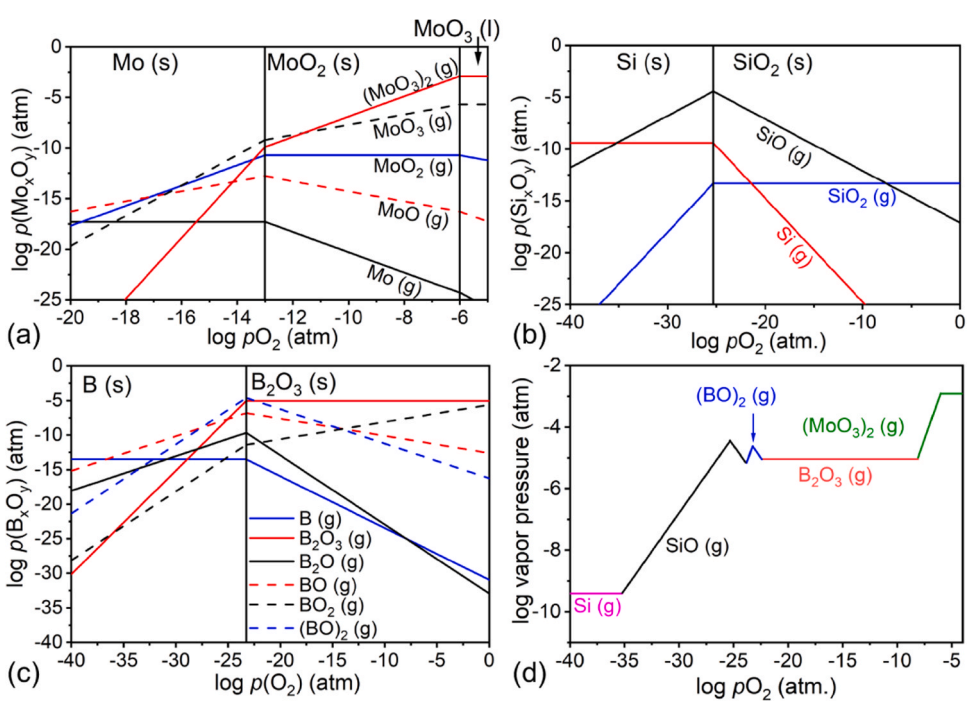

Fig. 3. Stability diagrams at 1100 °C for: (a) Mo–O, (b) Si–O, (c) B–O systems and (d) combined diagram presenting the species with the highest vapour pressure as a function of pO_2.

$$\frac{d\alpha}{dt} = Ae^{-\left(\frac{E_a}{RT}\right)} f(\alpha), \tag{4}$$

where A is the pre-exponential factor of the Arrhenius relation, E_a is the activation energy (J mol^{-1}), T is absolute temperature (K), R is the gas constant, $f(\alpha)$ represents the reaction model, and α is the conversion fraction. In a gravimetric measurement, α is defined by:

$$\alpha = \frac{m_t - m_0}{m_\infty - m_0}, \tag{5}$$

where m_0 denotes the initial mass, m_t is the mass at time t, and m_∞ is the mass after full conversion of the particles. Separating variables and integrating Eq. (4) gives the integral form of the isothermal rate law [35]:

$$g(\alpha) = kt, \tag{6}$$

where

$$g(\alpha) = \int_0^\alpha \frac{d(\alpha)}{f(\alpha)} \tag{7}$$

and

$$k = Ae^{\left(-\frac{E_a}{RT}\right)} \tag{8}$$

wherein $g(\alpha)$ is the integral reaction model and k being the rate constant.

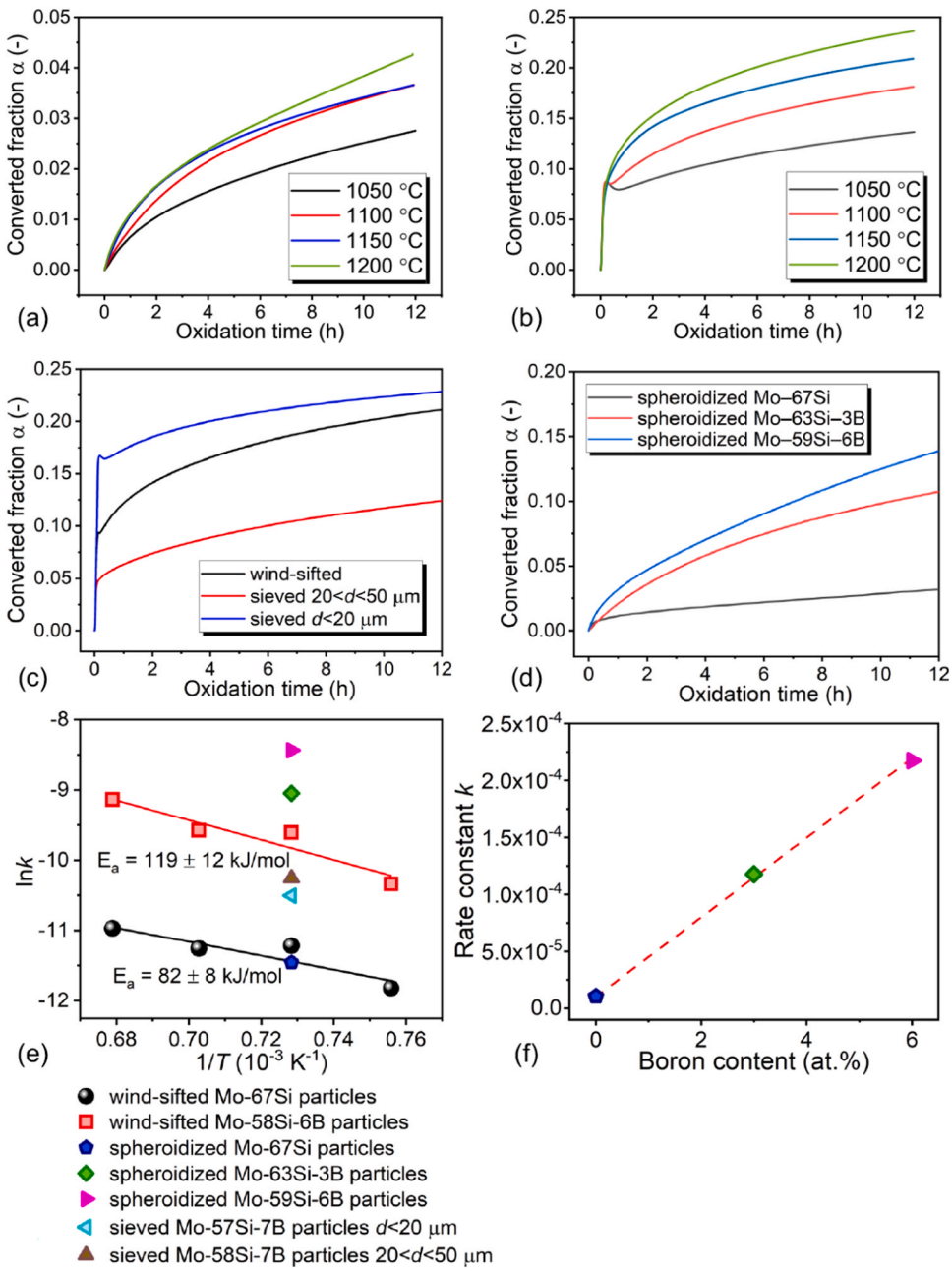

Fig. 4. Converted fraction α of (a) wind-sifted Mo–67Si particles and (b) wind-sifted Mo–58Si–6B particles after isothermal oxidation at between 1050 and 1200 °C in dry synthetic air for 12 hours; Converted fraction α of (c) Mo–Si–B particles with different particle sizes and (d) spheroidized Mo–Si based particles after isothermal oxidation at 1100 °C in dry synthetic air for 12 hours; the rate constant (e) ln k versus the inverse of absolute temperature ($1/T$) for all tested Mo–Si based particles and (f) k as a function of the boron content in the spheroidized Mo–Si based particles.

An experimental value for the rate constant k at different temperatures can be obtained from plotting $g(\alpha)$ versus t, once the kinetic model is established. The activation energy E_a and the frequency factor A can be estimated from ln k versus the reciprocal temperature (1/T).

The relative mass change ($\Delta m/m_0$) as recorded with thermogravimetry during the isothermal high temperature oxidation was used to determine the fraction of $MoSi_2$ based particles converted into oxidation products as a function of temperature and time. After the surface of the $MoSi_2$ based particles is covered with an oxide layer, the chemical reaction according to Eq. (1) is dominant [13,14,19]. Then, it holds that:

$$m_\infty/m_0 = \left(M_{Mo_5Si_3} + 7M_{SiO_2}\right)/5M_{SiO_2}, \tag{9}$$

where M is the corresponding molar mass.

3.2.1. Effect of boron addition

The converted fraction (α) of wind-sifted Mo–67Si particles from $MoSi_2$ to SiO_2 is rather small during oxidation in the temperature range of 1050 up to 1200 °C; see Fig. 4a. But an increased conversion with increasing temperature can be clearly observed; see Fig. 4a.

The wind-sifted Mo–58Si–6B particles results in a much larger amount of silica formed upon oxidation in the temperature range of 1050 up to 1200 °C; see Fig. 4b. As compared to the oxidation of the Mo–67Si particles (Fig. 4a), the oxidation kinetics of the Mo–58Si–6B particles is strongly promoted by the addition of boron. Note that some weight loss can be observed at the initial oxidation stage of the boron doped $MoSi_2$ particles when oxidized at 1050 and 1100 °C; see Fig. 4b. This weight loss may also have happened at the higher oxidation temperatures, but is not seen because of the net weight increase. The weight loss during the initial stage of oxidation is associate with the formation of volatile species of MoO_3, which indicates that then the surface of the particles was not yet fully covered by a layer of SiO_2 (or borosilicate).

3.2.2. Effect of particle size

The converted fraction of the Mo–Si–B particles with different particle sizes upon oxidation in dry synthetic air in the temperature of 1100 °C is shown in Fig. 4c. As can be seen, the particles size has a significant effect on the initial oxidation; see Fig. 4c. Rapid initial oxidation followed by a steady-state oxidation can be observed for the particles containing fine fractions ($d < 20$ μm and wind-sifted particles containing various particle sizes); see Fig. 4c. The fine particles ($d < 20$ μm) exhibit the largest conversion after the oxidation process with the fastest initial weight gain followed by a weight loss during the initial stage. Particles with a size distribution of $20 < d < 50$ μm show the least conversion and a weight loss cannot be observed anymore. The weight loss is associated with the formation of volatile MoO_3 species as mentioned in Section 3.2.1. This suggests that the surface of the particles is rapidly fully covered with silica and sealing the alloy and preventing volatile species to form. Thus, the transition from the initial to the steady oxidation state is enhanced by reducing the particle surface area corresponding with increasing particle size.

3.2.3. Effect of boron content

The isothermal oxidation kinetics of the spheroidized Mo–Si–B particles with different boron addition, at 1100 °C in dry synthetic air, in terms of the conversion of $MoSi_2$ upon oxidation is displayed in Fig. 4d. The conversion increased with increasing of boron addition, which further demonstrated the enhanced oxidation of $MoSi_2$ by a minor addition of boron.

3.2.4. Effect of particle microstructure

It is remarkable that the quick weight gain and the subsequent weight loss stage cannot be observed for these spherical particles with refined microstructure; cf. Fig. 4d. Apparently, the protective silica or borosilicate layer is rapidly formed when the boron containing phase is homogeneously distributed and particles are spherical and smooth. Hence, the transition from the initial fast to the steady-state oxidation state is further promoted.

3.3. Kinetic model

When a continuous oxide scale is formed on the surface of the particles, two possible oxygen migration mechanism may occur in the oxide scale [36]; namely: (i) molecular permeation through the channels of open space in the low-density structures and (ii) atomic oxygen self-diffusion through the network of bonded oxygen by making use of lattice vacancies and interstitial positions. At high temperatures, these two kinds of diffusions can act simultaneously, which is a so called "interstitialcy diffusion" process. In this process, the presence of O_2 is required as an interstitial defect or "carrier" for the self-diffusion of oxygen. For diffusion-controlled solid-state reactions, the thermally activated oxidation process can be described best with the 3-D diffusion-Jander (D3) model [18,35,37] based on the assumption of spherical solid particles:

$$g(\alpha) = \left(1 - (1-\alpha)^{1/3}\right)^2. \tag{10}$$

When combining Eqs. (4)–(6) and Eq. (10), then the expression representing the converted fraction α can be calculated as:

$$\alpha = 1 - \left(1 - \sqrt{kt}\right)^3. \tag{11}$$

The D3 model was fitted to the conversion data pertaining to the steady-state oxidation stage; see Fig. S2 in Supplementary Material. Comparison between the model and experimental data confirms that the D3 model describes well the oxidation kinetics of the $MoSi_2$ based particles in the steady-state oxidation.

The rate constant k is determined form a linear least-square fitting of Eq. (4)(6) to the kinetic data at each isothermal oxidation; see Fig. 4e. The activation energy of the oxidation reaction of wind-sifted particles with and without boron addition is evaluated from the slope of a line a linear least-square fitted through the data of ln k versus the reciprocal of absolute temperature (1/T); see Fig. 4e. The activation energy equals to 82 ± 8 kJ/mol for the oxidation in the steady state of wind-sifted Mo–67Si particles, which is the same to the reported activation energy of oxygen transport through pure SiO_2 prepared by a gel process [38]. For the wind-sifted Mo–58Si–6B particles, the oxidation activation energy equals to 119 ± 12 kJ/mol, which corresponds well to the activation energy of oxygen diffusion in boron containing glasses (118 kJ/mol for low boron content) [38]. These values are close to the activation energies of the "interstitialcy diffusion" process (85–121 kJ/mol) [36], indication a simultaneous diffusion process of molecular O_2 and atomic O in the oxide scale formed on Mo–Si(–B) particles. The increased activation energy is likely related to the changing of the SiO_2 structure by boron addition [27,38]. Large B_5O_6-ring segments build up inside the silica network, which increases the oxygen permeation [27,36,38]. The diffusion behavior by the exchange of network oxygen with interstitially dissolved O_2 is therefore also increased, which requires a higher activation energy [36,39]. By increasing the boron content from 0 to 3 and 6 at.% of the spheroidized Mo–Si–B particles, the rate constant in the steady-state oxidation increases proportionally; see Fig. 4f. This demonstrates that the accelerated oxidation can be attributed to the addition of boron.

Although particle size has shown a significant effect on the initial oxidation, it has little effect on the steady-state oxidation of the $MoSi_2$ based particles. The oxide growth rate constant k is almost the same for the Mo–67Si particles after spheroidization and the wind-sifted Mo–67Si particles with irregular shape; see Fig. 4e. Also, not much differences can be observed among the oxide growth rate constant k of Mo–Si–B particles with different particle sizes, namely wind-sifted particle with various particle size, fine particles with $d < 20$ μm and particles with $20 < d < 50$ μm.

The microstructure of the $MoSi_2$ particles with boron addition, on the contrary, has a significant effect on the rate constant of steady-state oxidation. The rate constant of oxidation of Mo–Si–B particles increased from 3.5×10^{-5} s^{-1} (sieved Mo–58Si–7B particles with $20 < d < 50$ μm) to 2.2×10^{-4} s^{-1} (spheroidization Mo–59Si–6B particles, $20 < d < 50$ μm) by refining the boron distribution. For this reason, the diffusion distances of boron are reduced, and the boron contained in the borosilicate covering the particles will diffuse more quickly into the structure and promote the formation of continuous passive layer. A shortened transient oxidation stage of Mo–Si–B alloy by a refined microstructure was also observed; cf. [40].

3.4. Oxide scale microstructure

After oxidation at 1100 °C for 20 hours in dry synthetic air, the oxide scale was formed around the core particles in the spheroidized particles; see Fig. 5a–c. The surface of the particles with B addition has a smoother appearance than that of the spheroidized Mo–67Si particles after oxidation; see Fig. 5d–f.

Cross-sections of spheroidized Mo–67Si particles after oxidation at 1100 °C for 20 hours in dry synthetic air show that a thin but uniform layer of silica was formed; see Fig. 5g. After similar oxidation of $MoSi_2$ particles with boron addition, thicker oxide layers were observed indicating an enhanced oxidation by the boron addition, which is consistent with the oxidation kinetics captured by TGA in Section 3.2.3. The oxide scale formed on $MoSi_2$ particles with boron addition is rather uneven as compared with oxidized pure $MoSi_2$ particles; see Fig. 5g–i. The borosilicate oxide scale formed on boron-doped $MoSi_2$ particles exhibits higher flowability due to its higher viscosity. Since the particles were stacked during the oxidation experiment with TGA, borosilicate formed by the oxidation of boron doped $MoSi_2$ tends to flow and preferentially covering the free surfaces. The chemical composition and microstructure of the core of all the particles remained the same as before oxidation.

The enhanced oxidation by boron addition to the $MoSi_2$ particles is also manifest in the recorded diffractograms; see Fig. 6. With increasing boron content, the intensity of the $MoSi_2$ diffraction lines decreases,

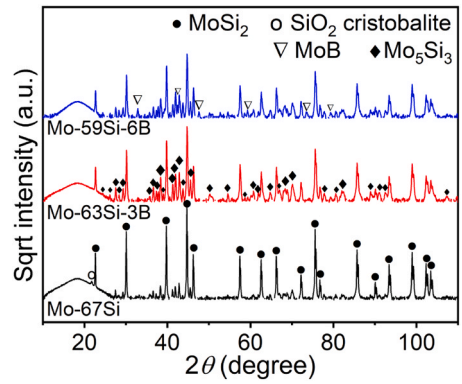

Fig. 6. X-ray diffraction patterns of the spheroidized Mo–Si based particles after isothermal exposure at 1100 °C for 20 hours in dry synthetic air.

while the intensity of the Mo_5Si_3 diffraction lines increases due to Si depletion. In addition, diffraction lines associated with cristobalite were observed in the diffractogram of spheroidized Mo–67Si particles after oxidation at 1100 °C in dry synthetic air for 20 hours, but not in the diffractograms of particles with boron addition. This indicates that the structure of the oxide scale is changed by the introduction of boron. A crystalline structure with twin lamellae can be seen clearly in the oxide scale formed on spheroidized Mo–67Si particles (cf. Fig. 7a), while the crystalline structure cannot be observed in the oxide scale formed on spheroidized Mo–59Si–6B particles (cf. Fig. 7b). The twin lamellae structure is a characteristic microstructural features of cristobalite [41]. However, a selected area diffraction pattern cannot be obtained of these cristobalite areas due to high diffuse electron scattering intensities [41]. Evidence of such a transition from crystalline to amorphous structure of the oxide scale was captured with TEM, while operating with the electron beam at 200 keV; see Video S1 in Supplementary Material. In order to confirm the crystalline structure, lattice plane imaging was performed quickly with high resolution TEM (HRTEM) near the interface of the oxide scale and the $MoSi_2$ substrate; see Fig. 7c. Fast Fourier

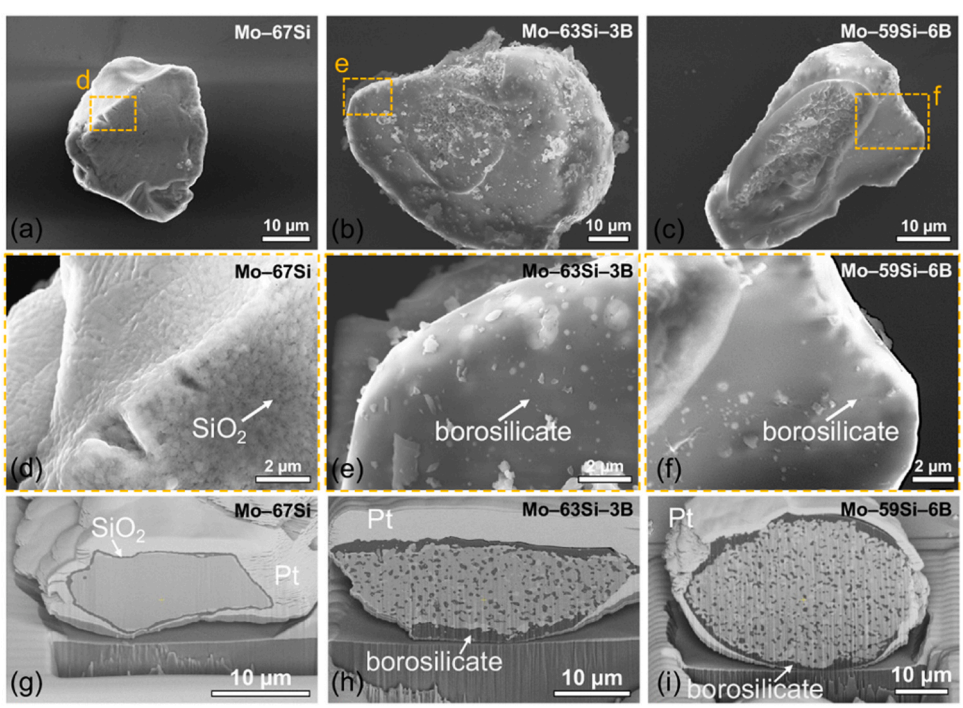

Fig. 5. SEM images of the surface and cross-section of spheroidized Mo–Si based particles after isothermal exposure at 1100 °C for 20 hours in synthetic air: (a)(d)(g) Mo–67Si particles, (b)(e)(h) Mo–63Si–3B particles and (c)(f)(i) Mo–59Si–6B particles.

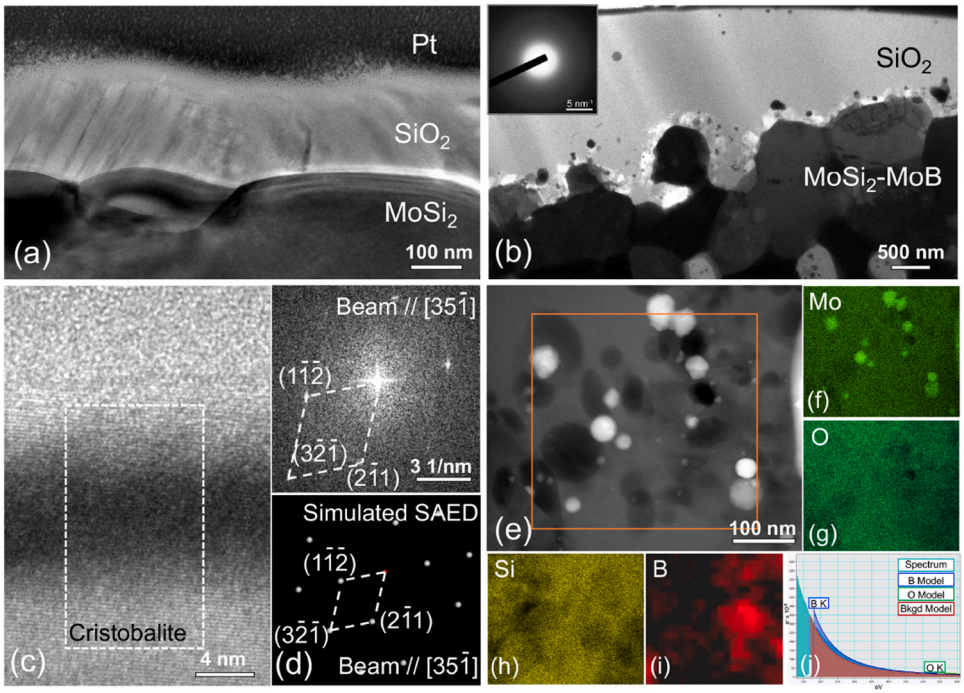

Fig. 7. TEM image of the oxide scale grown on (a) spheroidized Mo–67Si particles; (b) spheroidized Mo–59Si–6B particles; (c) HRTEM image of SiO_2-$MoSi_2$ interface on spheroidized Mo–67Si particle; (d) FFT of white box in (c) and simulated SAED by PDF-4+ software (version 2023) showing the orientation of cristobalite atomic layers; (e) HAADF image of the inclusion near the interface of the oxide scale and substrate in (b) and (f)–(h) the corresponding X-ray emission maps of Mo, O and Si respectively; EELS (i) elemental map and (j) spectrum of boron corresponding to the reduced area in (e).

Transformation (FFT) was performed on the lattice fringes and the obtained pattern matches well with the simulated diffraction pattern of tetragonal cristobalite; see Fig. 7d. The glassy oxide scales formed on spheroidized Mo–58Si–6B particles contains inclusions near the interface of the oxide scale and the inner core material; see Figs. 7b and 7e. The bright nano particles are Mo rich and likely composed of MoO_3. The presence of boron in these inclusions was confirmed by Electron Energy Loss Spectroscopy (EELS); see Figs. 7i and 7j. As can be seen, the peak associated with boron is clearly present in the EELS spectrum (Fig. 8j). The distribution of boron in the oxide scale corresponds with the dark inclusions; see Figs. 7e and 7i.

3.5. Oxygen transport through oxide scale

Upon oxidation, the MoB_x in the alloy is oxidized resulting in B_2O_3, which dissolves in SiO_2 as a network modifier. Then, some Si–O bonds are broken and borosilicate is formed, which is beneficial for vitrification and hinders crystallization of SiO_2. Easier transport of oxygen through amorphous borosilicate makes it less passive than the crystalline silica scale formed on pure $MoSi_2$ [36,42], which explains the accelerated oxidation by boron addition to $MoSi_2$ during the steady-state oxidation.

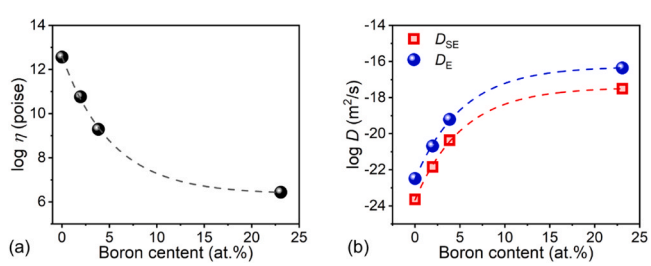

Fig. 8. (a) Viscosity of SiO_2–B_2O_3 glass as a function of boron content at 1100 °C estimated using viscosity data reported by Yan *et al.* [45]; (b) oxygen diffusivity calculated with Stokes-Einstein (D_{SE}) and Eyring equation (D_E).

Two relations were reported to present the oxygen migration in an amorphous oxide scale at high temperatures, viz.: (i) Stokes-Einstein and Eyring equation [36,43,44]. Stokes-Einstein equation, expressed as Eq. (12), which was used to estimate the diffusion of oxygen molecule in SiO_4 tetrahedral network and (ii) Eyring equation, expressed as Eq. (13), considers oxygen diffused in the form of ions.

$$D = \frac{kT}{6\pi r\eta} \tag{12}$$

and

$$D = \frac{kT}{\lambda\eta}, \tag{13}$$

where k is the Boltzmann constant, T the thermodynamic temperature and r is particle radius through glass (0.121 nm, the distance of O–O bond in O_2) and λ is the average jump distance of diffusion species (0.159 nm, the distance of Si–O bond in SiO_2) [36,43]. As mentioned in Section 3.3., these two kinds of diffusion types act simultaneously and are linked to each other through so-called "interstitialcy diffusion" [20].

Both the Stokes-Einstein and the Eyring equation expresses that the oxygen permeability is inversely proportional to the glass viscosity. Yan *et al.* measured the viscosity of a series of silica with different B contents in their sintering study [45]. Using their viscosity data, the relationship of the change in viscosity of borosilicate glass as a function of B content at 1100 °C is constructed in Fig. 8a and the diffusivity of oxygen was calculated using the Stokes-Einstein as well as the Eyring equation, respectively; see Fig. 8b. It can be seen that the introduction of a trace amount of boron can reduce the viscosity of SiO_2 by several orders of magnitude (see Fig. 8a), which makes the diffusion coefficient of oxygen to increases by several orders of magnitude; see Fig. 8b. This increase of the oxygen diffusion coefficient explains the enhanced growth of the oxide scale on the $MoSi_2$ particles by the B addition.

4. Conclusions

The oxidation of $MoSi_2$ and $MoSi_2$–MoB_x particles follows a two-step oxidation process, namely an initial fast oxidation followed by a relatively slow steady-state oxidation. The formation of a continuous protective scale on the surface marks the transition from the initial fast to the steady-state oxidation of $MoSi_2$ based particles. The oxidation kinetics in the steady-state stage can be described with a 3-D diffusion-Jander (D3) reaction model.

The high temperature oxidation kinetics of $MoSi_2$ particles is significantly enhanced when boron is added. The oxidation rate constant pertaining to the steady-state stage of the $MoSi_2$ based particles increases proportional with their boron content (observed at 1100 °C).

The particles size of Mo–Si–B particles has a significant effect on the initial fast oxidation but has little effect on the steady-state of the oxidation at 1100 °C in dry synthetic air. The transition from the initial to steady-state oxidation state is accelerated when the particles become larger due to the reduced surface area. The transition from the initial to steady-state oxidation is further promoted when the boron containing phase is finer dispersed.

Microstructure analysis of the oxide scaled formed on these particles reveals that the formation of crystalline SiO_2 is mitigated while amorphous borosilicate is promoted by the addition of boron. The MoB phase in the particle alloy is oxidized to B_2O_3, which dissolves into SiO_2 as a network modifier causing vitrification of the oxide scale.

The enhanced oxidation of $MoSi_2$ particles by boron addition is due to an increase of the diffusion coefficient of oxygen in the borosilicate oxide scale, which is inversely proportional to its viscosity.

CRediT authorship contribution statement

Zhaoying Ding: Formal analysis, Investigation, Visualization, Writing – original draft. **Xiyu Yao:** Formal analysis, Investigation, Writing – review & editing. **Johannes Brouwer:** Formal analysis, Investigation, Writing – review & editing. **Willem Sloof:** Conceptualization, Project administration, Resources, Supervision, Writing – review & editing. **Marcel Hermans:** Resources, Supervision, Writing – review & editing. **Jia-Ning Zhu:** Formal analysis, Investigation, Writing – review & editing. **Vera Popovich:** Resources, Supervision, Writing – review & editing.

Declaration of Competing Interest

The authors declare that they have no known competing financial interests or personal relationships that could have appeared to influence the work reported in this paper.

Data Availability

Data will be made available on request.

Acknowledgement

This project has received funding from European Union Seventh Framework Programme (FP7/2007-2013) under grant agreement No. 309849, SAMBA. China Scholarship Council is acknowledged by Zhaoying Ding for their support (Grant No. 201806120145). The authors thank Ing. R.W.A. Hendrikx for the XRD analysis, Ing. M.M. van den Brink for the ICP-OES analysis.

Appendix A. Supporting information

Supplementary data associated with this article can be found in the online version at doi:10.1016/j.jeurceramsoc.2024.05.002.

References

[1] J.H. Perepezko, Surface Engineering of Mo-Base Alloys for Elevated-Temperature Environmental Resistance, Annu. Rev. Mater. Res. 45 (1) (2015) 519–542, https://doi.org/10.1146/annurev-matsci-070214-020959.

[2] X.D. Tian, X.P. Guo, Z.P. Sun, J.L. Qu, L.J. Wang, Oxidation resistance comparison of $MoSi_2$ and B-modified $MoSi_2$ coatings on pure Mo prepared through pack cementation, Mater. Corros. 66 (7) (2015) 681–687, https://doi.org/10.1002/maco.201407631.

[3] K. Nagata, S.C. Deevi, Oxidation behavior of molybdenum silicides and their composites, Intermetallics 8 (2000) 1147–1158, https://doi.org/10.1016/S0966-9795(00)00060-1.

[4] Z. Derelioglu, A.L. Carabat, G.M. Song, S. v.d. Zwaag, W.G. Sloof, On the use of B-alloyed $MoSi_2$ particles as crack healing agents in yttria stabilized zirconia thermal barrier coatings, J. Eur. Ceram. Soc. 35 (16) (2015) 4507–4511, https://doi.org/10.1016/j.jeurceramsoc.2015.08.035.

[5] F. Nozahic, C. Estournès, A.L. Carabat, W.G. Sloof, S. van der Zwaag, D. Monceau, Self-healing thermal barrier coating systems fabricated by spark plasma sintering, Mater. Des. 143 (2018) 204–213, https://doi.org/10.1016/j.matdes.2018.02.001.

[6] Y. Chen, X. Zhang, S. van der Zwaag, W.G. Sloof, P. Xiao, Damage evolution in a self-healing air plasma sprayed thermal barrier coating containing self-shielding $MoSi_2$ particles, J. Am. Ceram. Soc. 102 (8) (2019) 4899–4910, https://doi.org/10.1111/jace.16313.

[7] J. Krishnasamy, S.A. Ponnusami, S. Turteltaub, S. van der Zwaag, Modelling the fracture behaviour of thermal barrier coatings containing healing particles, Mater. Des. 157 (2018) 75–86, https://doi.org/10.1016/j.matdes.2018.07.026.

[8] S.A. Ponnusami, J. Krishnasamy, S. Turteltaub, S. Zwaag, A micromechanical fracture analysis to investigate the effect of healing particles on the overall mechanical response of a self-healing particulate composite, Fatigue Fract. Eng. Mater. Struct. 42 (2) (2018) 533–545, https://doi.org/10.1111/ffe.12929.

[9] F. Nozahic, A.L. Carabat, W. Mao, D. Monceau, C. Estournes, C. Kwakernaak, S. van der Zwaag, W.G. Sloof, Kinetics of zircon formation in yttria partially stabilized zirconia as a result of oxidation of embedded molybdenum disilicide, Acta Mater. 174 (2019) 206–216, https://doi.org/10.1016/j.actamat.2019.05.046.

[10] P. Greil, Generic principles of crack-healing ceramics, J. Adv. Ceram. 1 (4) (2012) 249–267, https://doi.org/10.1007/s40145-012-0020-2.

[11] T. Osada, K. Kamoda, M. Mitome, T. Hara, T. Abe, Y. Tamagawa, W. Nakao, T. Ohmura, A novel design approach for self-crack-healing structural ceramics with 3D networks of healing activator, Sci. Rep. 7 (1) (2017) 17853, https://doi.org/10.1038/s41598-017-17942-6.

[12] J. Chen, C. Li, Z. Fu, X. Tu, M. Sundberg, R. Pompe, Low temperature oxidation behavior of a $MoSi_2$-based material, Mater. Sci. Eng., A 261 (1999) 239–244, https://doi.org/10.1016/S0921-5093(98)01071-5.

[13] Y.Q. Liu, G. Shao, P. Tsakiropoulos, On the oxidation behaviour of $MoSi_2$, Intermetallics 9 (2001) 125–136, https://doi.org/10.1016/S0966-9795(00)00114-X.

[14] S. Knittel, S. Mathieu, M. Vilasi, The oxidation behaviour of uniaxial hot pressed $MoSi_2$ in air from 400 to 1400 °C, Intermetallics 19 (8) (2011) 1207–1215, https://doi.org/10.1016/j.intermet.2011.03.029.

[15] Y. Yang, M. Li, L. Xu, J. Xu, Y. Qian, J. Zuo, T. Li, Oxidation behaviours of ZrB_2-SiC-$MoSi_2$ composites at 1800 °C in air with different pressures, Corros. Sci. 157 (2019) 87–97, https://doi.org/10.1016/j.corsci.2019.05.027.

[16] M. Samadzadeh, C. Oprea, H. Karimi Sharif, T. Troczynski, Comparative studies of the oxidation of $MoSi_2$ based materials: High-temperature oxidation (1000–1600 °C), Int. J. Refract. Met. Hard Mater. 69 (2017) 31–39, https://doi.org/10.1016/j.ijrmhm.2017.07.015.

[17] Z. Ding, J.C. Brouwer, C. Kwakernaak, M.J.M. Hermans, V. Popovich, W. J. Quadakkers, W.G. Sloof, Selective oxidation of aluminium in $Mo(Al,Si)_2$, Corros. Sci. 211 (2023), https://doi.org/10.1016/j.corsci.2022.110884.

[18] Z. Ding, J.C. Brouwer, C. Kwakernaak, J.-N. Zhu, V. Popovich, M.J.M. Hermans, W. G. Sloof, $Mo(Al_xSi_{1-x})_2$ healing particles for high temperature ceramics and encapsulation by selective oxidation of aluminium, Mater. Des. 225 (2023), https://doi.org/10.1016/j.matdes.2022.111577.

[19] Y.T. Zhu, M. Stan, S.D. Conzone, D.P. Butt, Thermal Oxidation Kinetics of MoSi2-Based Powders, J. Am. Ceram. Soc. 82 (10) (1999) 2785–2790, https://doi.org/10.1111/j.1151-2916.1999.tb02156.x.

[20] Y.T. Zhu, L. Shu, Kinetics and products of molybdenum disilicide powder oxidation, J. Am. Ceram. Soc. 85 (2) (2002) 507–509, https://doi.org/10.1111/j.1151-2916.2002.tb00124.x.

[21] J.A. Lemberg, R.O. Ritchie, Mo-Si-B alloys for ultrahigh-temperature structural applications, Adv. Mater. 24 (26) (2012) 3445–3480, https://doi.org/10.1002/adma.201200764.

[22] A. Lange, R. Braun, Magnetron-sputtered oxidation protection coatings for Mo–Si–B alloys, Corros. Sci. 84 (2014) 74–84, https://doi.org/10.1016/j.corsci.2014.03.013.

[23] S. Majumdar, B. Dönges, B. Gorr, H.-J. Christ, D. Schliephake, M. Heilmaier, Mechanisms of oxide scale formation on yttrium-alloyed Mo–Si–B containing fine-grained microstructure, Corros. Sci. 90 (2015) 76–88, https://doi.org/10.1016/j.corsci.2014.09.017.

[24] H. Yokota, T. Kudoh, T. Suzuki, Oxidation resistance of boronized $MoSi_2$, Surf. Coat. Technol. 169-170 (2003) 171–173, https://doi.org/10.1016/S0257-8972(03)00221-4.

[25] A. Lange, M. Heilmaier, T.A. Sossamann, J.H. Perepezko, Oxidation behavior of pack-cemented Si–B oxidation protection coatings for Mo–Si–B alloys at 1300°C, Surf. Coat. Technol. 266 (2015) 57–63, https://doi.org/10.1016/j.surfcoat.2015.02.015.

[26] S.H. Wen, C.G. Zhou, J.B. Sha, Improvement of oxidation resistance of a Mo-62Si-5B (at%) alloy at 1250 °C and 1350 °C via an in situ pre-formed SiO_2 fabricated by spark plasma sintering, Corros. Sci. 127 (2017) 175–185, https://doi.org/10.1016/j.corsci.2017.08.019.
[27] Z. Ding, J.C. Brouwer, J.-N. Zhu, V. Popovich, M.J.M. Hermans, W.G. Sloof, Effects of boron addition on the high temperature oxidation of MoSi2 alloys, Scr. Mater. 234 (2023), https://doi.org/10.1016/j.scriptamat.2023.115580.
[28] Y. Danzaki, K. Wagatsuma, T. Syoji, K. Yoshimi, Dissolution of molybdenum-silicon (-boron) alloys using a mixture of sulfuric, nitric and hydrofluoric acids and a sequential correction method for ICP-AES analysis, Fresenius' J. Anal. Chem. 369 (2001) 184–186, https://doi.org/10.1007/s002160000616.
[29] G.A. Sweet, M. Brochu, R.L. Hexemer, I.W. Donaldson, D.P. Bishop, Microstructure and mechanical properties of air atomized aluminum powder consolidated via spark plasma sintering, Mater. Sci. Eng.: A 608 (2014) 273–282, https://doi.org/10.1016/j.msea.2014.04.078.
[30] J.-N. Zhu, Z. Ding, E. Borisov, X. Yao, J.C. Brouwer, A. Popovich, M. Hermans, V. Popovich, Healing cracks in additively manufactured NiTi shape memory alloys, Virtual Phys. Prototyp. 18 (1) (2023) e2246437, https://doi.org/10.1080/17452759.2023.2246437.
[31] D.V. Rybkovskiy, A.G. Kvashnin, Y.A. Kvashnina, A.R. Oganov, Structure, stability, and mechanical properties of boron-rich Mo-B phases: a computational study, J. Phys. Chem. Lett. 11 (7) (2020) 2393–2401, https://doi.org/10.1021/acs.jpclett.0c00242.
[32] M.J. Kriegel, W. Foerster, D. Chmelik, O. Fabrichnaya, J. Januschewsky, M. Kathrein, L.S. Sigl, D. Rafaja, Diffusion path and growth of intermediate phases in Mo/(Si,B) diffusion couples, 18th Plansee Seminar (2013). https://doi.org/10.13140/RG.2.1.3233.0484.
[33] P.R. Taleghani, S.R. Bakhshi, M. Erfanmanesh, G.H. Borhani, R. Vafaei, Improvement of $MoSi_2$ oxidation resistance via boron addition: Fabrication of MoB/MoSi2 composite by mechanical alloying and subsequent reactive sintering, Powder Technol. 254 (2014) 241–247, https://doi.org/10.1016/j.powtec.2014.01.034.
[34] M.D. Johnston, L.T. Khajavi, M. Li, S. Sokhanvaran, M. Barati, High-temperature refining of metallurgical-grade silicon: a review, JOM 64 (8) (2012) 935–945, https://doi.org/10.1007/s11837-012-0384-3.
[35] A. Khawam, D.R. Flanagan, Solid-state kinetic models: basics and mathematical fundamentals, J. Phys. Chem. B 110 (35) (2006) 17315–17328, https://doi.org/10.1021/jp062746a.
[36] M.A. Lamkin, F.L. Riley, Oxygen mobility in silicon dioxide and silicate glasses: a review, J. Eur. Ceram. Soc. 10 (1992) 347–367, https://doi.org/10.1016/0955-2219(92)90010-B.
[37] L. Boatemaa, J.C. Brouwer, S. van der Zwaag, W.G. Sloof, The effect of the TiC particle size on the preferred oxidation temperature for self-healing of oxide ceramic matrix materials, J. Mater. Sci. 53 (8) (2018) 5973–5986, https://doi.org/10.1007/s10853-017-1973-x.
[38] J. Schlichting, Oxygen transport through glass layers fromed by a gel process, J. Non-Cryst. Solids 63 (1984) 173–181, https://doi.org/10.1016/0022-3093(84)90396-X.
[39] Z. Chen, W. Shao, M. Li, Z. Wu, P. Peng, C. Zhou, Effect of minor B modification on the oxidation behavior of $MoSi_2$ alloy at high temperature, Corros. Sci. 216 (2023), https://doi.org/10.1016/j.corsci.2023.111070.
[40] F.A. Rioult, S.D. Imhoff, R. Sakidja, J.H. Perepezko, Transient oxidation of Mo–Si–B alloys: Effect of the microstructure size scale, Acta Mater. 57 (15) (2009) 4600–4613, https://doi.org/10.1016/j.actamat.2009.06.036.
[41] C.-h Chao, H.-y Lu, β-Cristobalite stabilization in (Na_2O + Al_2O_3)-added silica, Metall. Mater. Trans. A 33 (2002) 2703–2711, https://doi.org/10.1007/s11661-002-0392-y.
[42] J.S. Park, R. Sakidja, J.H. Perepezko, Coating designs for oxidation control of Mo-Si-B alloys, Scr. Mater. 46 (2002) 765–770, https://doi.org/10.1016/S1359-6462(02)00070-2.
[43] L. Wang, W. Wang, Q. Fu, The improvement of the self-healing ability of $MoSi_2$ coatings at 900–1200 °C by introducing SiB_6, J. Eur. Ceram. Soc. 40 (8) (2020) 2896–2906, https://doi.org/10.1016/j.jeurceramsoc.2020.01.048.
[44] M.L.F. Nascimento, E.D. Zanotto, Mechanisms and dynamics of crystal growth, viscous flow, and self-diffusion in silica glass, Phys. Rev. B 73 (2) (2006), https://doi.org/10.1103/PhysRevB.73.024209.
[45] M.F. Yan, S.R. Macchesney, S.R. Nagel, W.W. Rhodes, Sintering of optical waveguide glasses, J. Mater. Sci. 15 (1980) 1371–1378, https://doi.org/10.1007/BF00752116.